Statistical analysis of spatial frequency supercontinuum in pattern forming feedback systems

Eric Louvergneaux,[*] Vincent Odent,[†] Mikhail I. Kolobov, and Majid Taki

Université Lille1, Laboratoire de Physique des Lasers, Atomes et Molécules, CNRS UMR 8523, 59655 Villeneuve d'Ascq Cedex, France
(Received 5 February 2013; published 3 June 2013)

We study numerically and experimentally the highly nonlinear dynamical regime (far above the primary instability threshold) of a one-dimensional spatially extended feedback system. The spatiotemporal dynamics is very complex and is characterized by the emission of a spatial frequency supercontinuum accompanied by the appearance of abnormally intense localized peaks in transverse patterns. We perform statistical analysis of this highly nonlinear regime in terms of the probability density function (PDF) of the peak intensities rather than usual tools such as correlation functions. We find that the statistics of these peak intensities is described very well by the generalized gamma (GG) probability density function and determine its three parameters which can be used as quantitative indicators of the transition from the weakly to the highly nonlinear regime. Most interestingly, we discover that in the highly nonlinear regime the GG PDF converges to the gamma probability density function with the shape parameter equal to 3/2. This limit corresponds to the Rayleigh probability density function of the peak amplitudes for the oceanic waves. This behavior of the PDF can be an indicator of the universality of the highly nonlinear regime for other processes involving supercontinua and chaos.

I. INTRODUCTION

Rogue events that are observed, e.g., in the open ocean in the form of rogue or freak waves [1–3], were predicted in optics [4], and in this context it has been proven that they can be controlled or even suppressed [5,6]. Very recently, such rogue events have been experimentally evidenced in optics in the regime of supercontinuum emission in fiber systems [6–9] and in spatially extended systems [10–14]. Observation of these rogue events in optics is not surprising since the self-focusing nonlinear Shrödinger equation (NLSE) reflects the temporal nonlinear dynamics of waves propagating in optical fibers [15] as well as on the ocean surface [1,16,17].

One of the main features of optical temporal rogue waves occurring in photonic crystal fibers is their inherent association with generation of an extremely broadband continuum of frequencies commonly called supercontinuum [7,18]. The dynamics of this highly nonlinear regime is very complex and the underlying physical processes are still under investigation [19–21]. In the spatiotemporal optical systems, highly nonlinear regimes are characterized by the spatiotemporal chaos, and the transition from the weakly nonlinear to highly nonlinear dynamics remains an open field of research [22–24]. It is natural to ask if in spatially extended systems the dynamics of the highly nonlinear regimes is also characterized by the emission of a continuum of spatial frequencies. Similarly, what features would the associated intense localized transverse structures share with that of optical temporal rogue waves? The prominent attributes of these latter events usually retained are the following [25]: their intensities are far greater than those associated with typical waves occurring in these systems (the criterion used in the oceanic rogue waves states that

their amplitude must exceed two times the significant wave height [1,17]); they disappear as fast as they appear [1,26]; and they occur very rarely as compared to the Gaussian statistics.

In this paper, we report on generation of spectral supercontinua (SC) in a one-dimensional transverse Kerr slice medium, subject to an optical feedback. We show that these supercontinua are closely related to generation of abnormally high intensity peaks in the transverse patterns that disappear as fast as they appear. The associated highly nonlinear regime [27] is far above the threshold for the Turing instability (spatial modulational instability), where stationary rolls are observed. We investigate this spatiotemporal chaotic regime using a statistical approach in terms of probability density functions (PDFs) of the pattern intensity maxima. We find that statistical distribution of these maxima is well described by the generalized gamma (GG) distribution, characterized by three parameters. These parameters are used as quantitative indicators to characterize the transition from the weakly to the highly nonlinear dynamical regime. In particular, we investigate the influence of the beam waist of the incident pump (specific to spatially extended optical systems) on the PDF.

Most interestingly, we discover that the GG PDF reduces to the gamma PDF with the shape parameter equal to 3/2 for the spatiotemporal chaotic regime very high above the Turing threshold. It should be noted that in terms of the probability density function for the peak amplitudes (instead of intensities) this corresponds to the Rayleigh distribution which was observed for the statistics of the oceanic waves. This behavior of the PDF can be an indicator of the universality of the spatiotemporal chaotic regime and calls for similar investigations in other types of dynamical systems manifesting chaos.

II. THE OPTICAL SYSTEM

The experimental setup used to observe optical spatial patterns is composed of a Kerr slice medium subjected to optical feedback [28]. It essentially consists in a nematic liquid crystal (LC) layer irradiated by a strong laser beam which is reflected back onto the sample by a simple plane mirror placed

---

*eric.louvergneaux@univ-lille1.fr; http://www.phlam.univ-lille1.fr/perso/louvergneaux/

†Present address: Departamento de Física, Facultad de Ciencias Físicas y Matemáticas, Universidad de Chile, Casilla 487-3, Santiago, Chile; vodent@ing.uchile.cl.
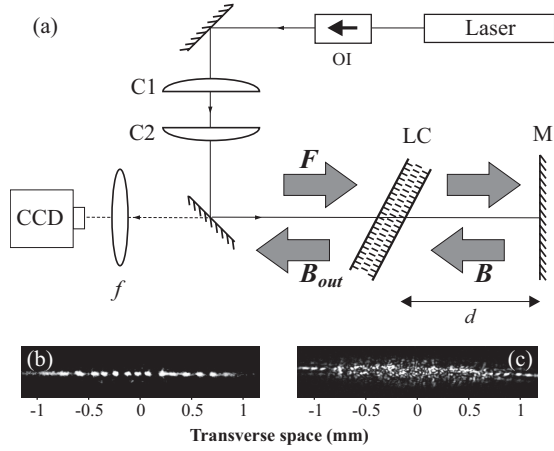
FIG. 1. (a) Schematic sketch of the experimental setup. LC, liquid crystal layer; M, feedback mirror; F, input optical field; B, backward optical field; d, feedback length. Typical one-dimensional experimental near-field patterns observed at (b) the Turing primary threshold and (c) at five times (intensity ratio) above this threshold in the highly nonlinear regime.

at a variable distance d from the LC layer [Fig. 1(a)]. The nonlinear medium is a 50-μm-thick layer of E_7 LC homeotropically anchored. The beam is delivered by a monomode frequency doubled Nd^{3+}:YVO$_4$ laser ($\lambda_0 = 532$ nm) which is shaped by means of two cylindrical telescopes in order to achieve a transverse quasimonodimensional (1D) pumping (beam diameters $\approx 240\ \mu$m $\times 3200\ \mu$m). The reflected beam is monitored after its second passage through the LC layer [B_{out} on Fig. 1(a)]. Near- and far-field distributions are simultaneously recorded. Two control parameters are easily accessible in the experiments, namely, the maximum intensity I_0 of the incident laser beam and the distance d between the mirror and the LC layer.

The reorientation of the LC director by the laser electric field leads to a nonlinear change of its refractive index which depicts pattern formation [29] above a primary threshold [Fig. 1(b)]. The spatiotemporal dynamics of the system is well described in the framework of a model introduced first by Akhmanov *et al.* [30] and later adapted by Firth and d'Alessandro [29]. In the 1D case it reads for the refractive index n of the nonlinear nematic LC layer,

$$\frac{\partial n}{\partial t} - \frac{\partial^2 n}{\partial x^2} + n = |F|^2 + |B|^2. \quad (1)$$

t and x are the time and space variables scaled with respect to the relaxation time τ and the diffusion length l_D of the liquid crystal. F and B are the forward and backward fields, respectively. Equation (1) must be completed by the two following equations that govern light propagation through the sample and over the feedback loop, respectively:

$$\frac{\partial(F,B)}{\partial z} = i\chi n(F,B), \quad (2)$$

$$\frac{\partial(F,B)}{\partial z} = \frac{-i}{2k_0}\nabla_\perp^2(F,B). \quad (3)$$

(F,B) means F or B. χ parametrizes the Kerr effect (positive for a focusing medium, $d > 0$) and k_0 is the laser field wave number. The profile of the forward propagation field

is assumed to be Gaussian so that $F(x) = F_0 \exp(-x^2/w^2)$, where w is the beam radius at LC sample.

$|B_{out}(x,t)|^2$ represents the variable we can access experimentally. This is the backward output optical beam intensity [$|B_{out}|^2$ on Fig. 1(a)] taken at the direct output of the LC sample. It is monitored on the near-field imaging CCD camera. It is our dynamical variable in this study and especially for the probability density functions. Using Eqs. (2) and (3), it reads

$$|B_{out}(x,t)|^2 = R\left|e^{i\chi n(x,t)}e^{i\sigma\nabla_\perp^2}[e^{i\chi n(x,t)}F(x)]\right|^2 \quad (4)$$

where R is the mirror intensity reflectivity. We have set $\sigma = d/k_0 l_D^2$, where d is the slice-mirror distance (Fig. 1). For simplicity, in the rest of the paper we will call it near-field intensity $I_{NF}(x)$ with $I_{NF}(x) \equiv |B_{out}(x,t)|^2$.

The rich variety of patterns appearing in this kind of system and their associated dynamics have been extensively investigated (see, e.g., [27,31–34]). Depending on the type of nonlinearity (quadratic, cubic, etc.) and the specific underlying system, many patterns have been reported ranging from rolls or hexagons to spatial solitons [35,36] and time-dependent patterns [37]. Most of these studies have been performed near threshold where amplitude equations, mainly Ginzburg-Landau and Swift-Hohenberg equations, can be derived to describe the weakly nonlinear dynamics above threshold [38]. Here, contrarily to these studies, our interest lies in the dynamics that occurs in strongly nonlinear regimes (far beyond threshold) where, unfortunately, order-parameter description in terms of amplitude equations fails. We now focus on the highly nonlinear dynamical regime where spatial spectrum enlargement and intense localized transverse pulses occur.

III. FROM STATIONARY MODULATIONAL INSTABILITY TO SPATIAL FREQUENCY CONTINUUM

The global features of the numerical scenarios of successive pattern destabilization in our system are the following: For low pumping intensity $I = |F_0|^2$, the output backward near field $|B_{out}(x,t)|^2$ simply reflects the overall Gaussian dependence of I. Further increase in the pump intensity leads to a critical situation where input intensity exactly compensates losses (dissipation). This is a marginal instability that is typical for nonequilibrium dissipative systems and is specific for the Turing instability. It is the counterpart of modulational instability in temporal systems [39]. At threshold $I = I_{th}$ ($F_{0\,th} = 0.86$), two spatial modes are marginally unstable with critical wave numbers $k = \pm k_{th} \simeq \pm 2\sqrt{\lambda d}$ [29]. Their signature at $I = 1.1 I_{th}$ are two peaks located at $k_{th} = \pm 0.061\ \mu$m^{-1} in the power spectrum of Fig. 2(e). The corresponding output transmitted near field B_{out} shows stationary rolls with a unique wavelength [Fig. 2(a)]. As the input power is increased beyond a secondary threshold I_d, these rolls destabilize via time pseudoperiodic dislocations associated with fringe annihilation (respectively, creation) for positive (respectively, negative) $2d$ values [28]. Further increasing the input intensity ($I = 4.4 I_{th}$), more spatial modes are destabilized due to multitongues of instability [27]. The spectrum shows multiple decreasing harmonics of the fundamental wave number k_{th} as can be seen in Fig. 2(f). The amplitudes of the sidebands then follow an exponential decay [inset of Fig. 2(f)]. The associated near-field distribution thus depicts sharp periodic
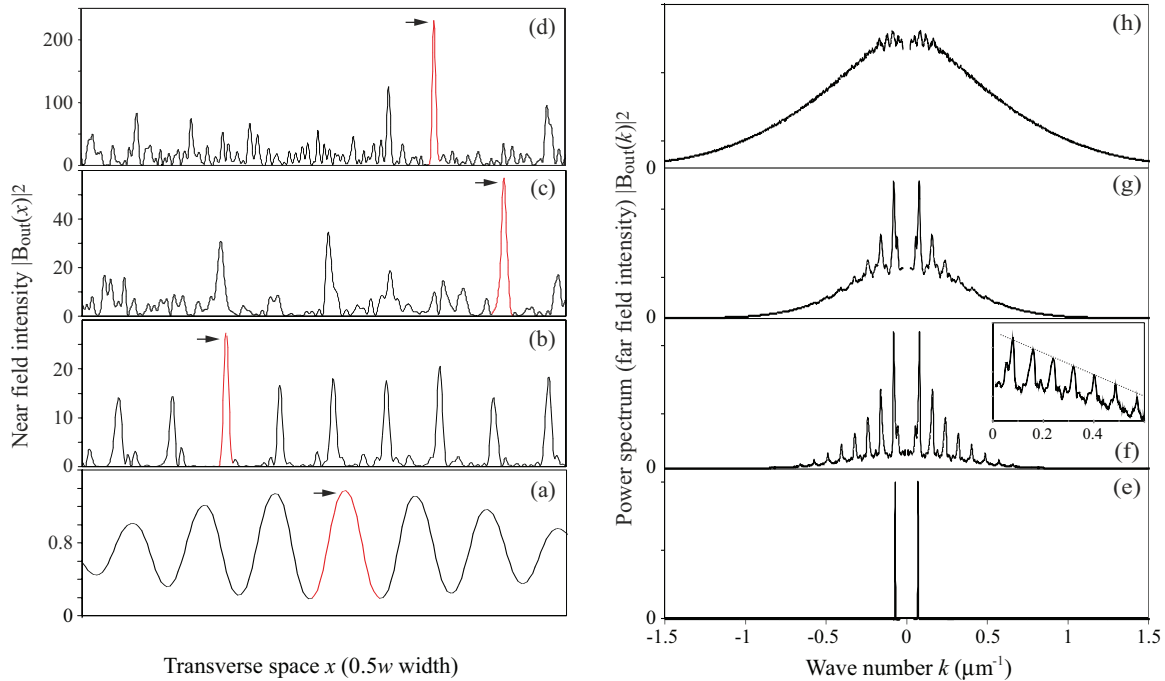
FIG. 2. (Color online) Evolution of the numerical [(a)–(d)] near- and [(e)–(h)] far-field (power spectrum) pattern profiles versus input field value F_0. [(a),(e)] $F_0 = 0.9$, $I/I_{th} = 1.1$; [(b),(f)] $F_0 = 1.8$, $I/I_{th} = 4.4$; [(c),(g)] $F_0 = 2.5$, $I/I_{th} = 8.4$; [(d),(h)] $F_0 = 4.5$, $I/I_{th} = 27.4$. $\sigma = 4.23$, $\chi = 1$, $d = 5$ mm, $R = 0.9$, $w = 1400$ μm. (a)–(d) are snapshots of the near-field evolution taken when the output intensity ($|B_{out}(x,t)|^2$) is maximum, whereas (e)–(h) are their corresponding time-averaged power spectra. Each peak (in red online) indicated by an arrow is then the highest peak of the total time recording of the associated numerical simulation. The inset in (f) is a close-up of the (f) spectra in $\log_{10}$ scale. For (e)–(h) plots, the $k = 0$ component has been suppressed and the power spectra rescaled.

peaks [Fig. 2(b)]. Continuing to increase the input laser power leads to a chaotic spatiotemporal dynamics [27] where the transverse cross section of the near field possesses no more regularity but the occurrence of intense localized structures [indicated by an arrow in Fig. 2(c)]. The corresponding spectrum broadens and leads to the appearance of a continuum of spatial frequencies that coexists with the previous primary wave number and its harmonics [Fig. 2(g)]. Finally, very far above the Turing threshold ($I/I_{th} = 27.4$) a full continuum of spatial frequencies is reached for the power spectrum [Fig. 2(h)]. The width of this continuous spectrum is approximately 20–30 times the initial modulational instability wave number $k_{th} \simeq 0.06$ μm^{-1} at primary threshold I_{th} [see Fig. 2(a)]. In this highly nonlinear regime, very intense localized peaks arise suddenly and erratically in the near-field pattern, as pointed out by an arrow in Fig. 2(d). We are interested in this highly nonlinear regime and its appearance from the modulational instability since it reminds one of emission of the supercontinuum in photonic fibers which is accompanied by optical rogue waves [7,9]. We adopt a statistical approach in terms of PDF for this analysis. Other issues such as the question of the coherence of the phenomenon [19,40,41] are currently in progress and are out of the scope of this paper.

IV. STATISTICAL ANALYSIS OF THE HIGHLY NONLINEAR REGIME USING PDFs

In the following, we associate the highly nonlinear regime to the presence and predominance of a spectral continuum

(similar to that of temporal chaotic or turbulent regimes) [Figs. 2(g) and 2(h)] that swamps the spectrum. We focus here on characterization of this regime in terms of the distribution of the maxima of the peak intensities in the near-field pattern. We evaluate the probability density functions of these peaks as for the supercontinuum analysis in fiber systems [6,7,9,11]. Our method is different from the previous approaches to study highly nonlinear regimes using correlation functions, time averaging, Karhunen-Loeve decomposition, etc. [22,23].

A. Typical PDF

The PDF represents the histogram of the intensity or the amplitude maxima distribution along the 1D near-field spatial pattern for a given recording time (a few hundreds of the relaxation time τ). Since the transverse profile of the pump is nonuniform, special care is taken for estimation of the PDF (see the Appendix). Starting from F_{th} (threshold for the modulational instability) and increasing F_0, the PDF continuously deforms from a localized region [Fig. 3(a)] (corresponding to the maxima of an almost sinusoidal spatial modulation) until it converges to a typical profile shown in Fig. 3(d). Thus, for supercontinuum emission, a typical PDF looks like the profile depicted in Fig. 3(d). It possesses an asymmetric bell shape with a long tail responsible for very big intensity fluctuations. An example of such a spatial intensity fluctuation is pointed out by an arrow in Fig. 2(d). It is interesting to note that a typical spatial PDF (Fig. 3) reminds one of some PDFs observed in the numerical simulations of the nonlinear Schrödinger equation (without higher-order
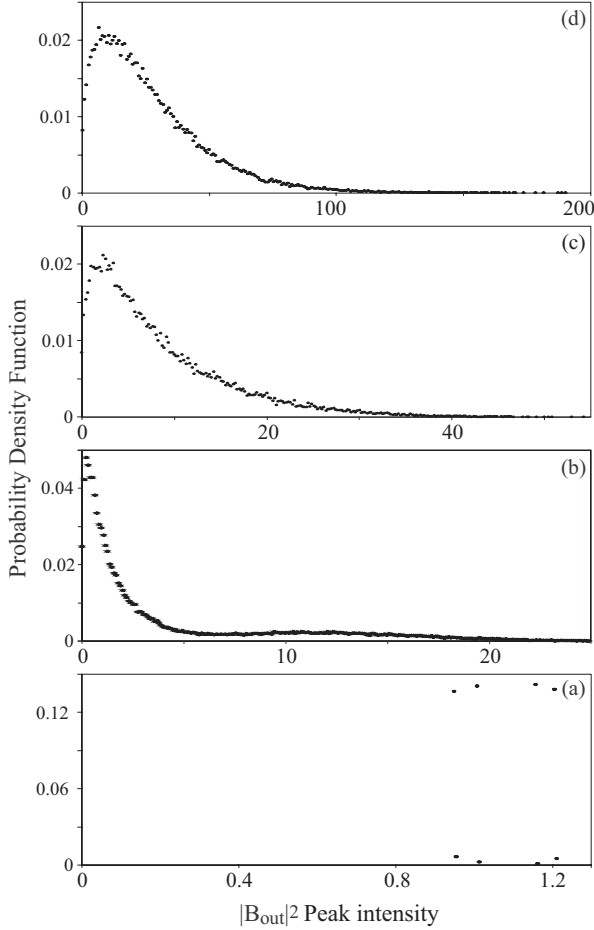
FIG. 3. Numerical PDFs of intensity peaks corresponding to the spectra of Fig. 2. Same parameters as Fig. 2. (a) $F_0 = 0.9$, $I/I_{th} = 1.1$; (b) $F_0 = 1.8$, $I/I_{th} = 4.4$; (c) $F_0 = 2.5$, $I/I_{th} = 8.4$; (d) $F_0 = 4.5$, $I/I_{th} = 27.4$.

dispersion terms or Raman effect) [see Fig. 14 in [42]], even if the physical mechanisms are different and the fiber system is conservative.

A log-linear plot of the previous PDFs (Fig. 4) shows that increasing the input pump value F_0 gives rise to more intense events without changing the global shape of the PDF tail in the highly nonlinear regime. It also shows that the tails seem to follow an exponential decreasing versus peak intensity. In the following sections we shall give a more detailed description of the features of PDF in the highly nonlinear regime.

B. PDFs analysis

Usually, to analyze the PDFs, and so the distribution of the intensity peaks in the near field, one can plot them in
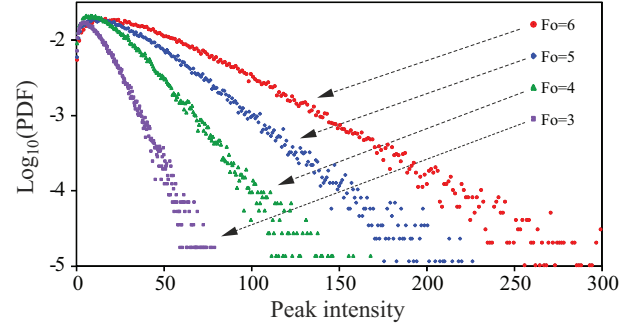

FIG. 4. (Color online) Evolution of the numerical PDF of intensity peaks for different pump intensity $I = |F_0|^2$ in $\log_{10}$ scale. Same parameters as Fig. 2.

log-linear scale for a direct reading of their departure from a Gaussian distribution, or calculate the higher-order moments of the distribution such as the skewness and kurtosis, which measure the asymmetry of the curve, or else compare the highest peaks to the significant ones. All these indicators provide information on the nature of the random events. We start first with the measure of the highest peaks corresponding to our supercontinuum.

1. Highest peaks

We saw previously that a typical PDF in the highly nonlinear regime possesses a long tail. This tail contains information about the strong and rare intensity peaks which arise in the transverse patterns. In oceanic waves, the way to estimate how strong the waves are is to calculate the ratio between the peak amplitude to the significant peak amplitude (commonly called H_s) [1]. When this ratio exceeds 2, the waves are referred to as freak or rogue. The significant amplitude is defined as follows: It is the average amplitude of the highest one-third (33.3%) amplitudes in the histogram of the PDF. Let us mention that the oceanic wave height corresponds to its amplitude, whereas in our case we will be dealing with intensities of the random peaks, i.e., amplitudes squared. In order to use the previous ratio, we will temporarily refer to PDFs versus peak amplitude and not peak intensity. In this case, one finds that the ratio between the highest peak amplitude to the significant peak amplitude reaches and can exceed 2 for (Table I). This corresponds to the regime of the emission of a full continuum of spatial frequencies [see Fig. 2(h)]. Moreover, these peaks appear and disappear in a very "short" time. Here, their lifetime is less than $\tau/2$ where τ is the relaxation time of the system. Thus, these highest peaks fill two of the three main criteria for rogue events. One can conclude that the emission of a continuum of spatial

TABLE I. Ratio between the highest peak amplitude ($|B_{out}|_{max}$) to the significant peak amplitude ($|B_{out}|_s$) corresponding to the numerical simulations of Fig. 2.

F_0	1.2	1.5	1.8	2	2.5	3	3.5	4	4.5	5	5.5	6
$|B_{out}|_s$	2.04	2.38	2.89	3.35	3.98	4.72	5.51	6.24	6.98	7.72	8.44	9.25
$|B_{out}|_{max}$	2.42	3.67	5.17	5.76	7.38	9.10	10.44	12.95	14.22	15.03	18.40	17.79
$\frac{|B_{out}|_{max}}{|B_{out}|_s}$	1.18	1.54	1.79	1.72	1.85	1.93	1.89	2.08	2.04	1.95	2.18	1.92

frequencies in the highly nonlinear regime is associated with the occurrence of very intense localized patterns.

To study more deeply the highly nonlinear regime and its emergence, we use a modelization of its statistical PDFs. This provides us with all the parameters of the statistical distribution that characterize quantitatively the probability law (asymmetric bell shape, long decreasing tail).

2. Modeling the PDF

Analytical probability density distributions of wave heights have been investigated in the literature on the oceanic rogue waves (see, e.g., [43,44]) and in very specific situations in the domain of optical rogue waves [45].

For oceanic random waves it can be argued that, following the central limit theorem, one can expect that the PDF of the wave amplitudes should be Gaussian in the limit of very small amplitudes. However, finite values of amplitudes result in small deviations of the PDF from the normal (Gaussian) distribution [43,44].

Since, *a priori*, in our case we expect to observe deviations from the normal distribution for our PDF, we have chosen to model the PDF by a GG distribution [46]. This distribution is very flexible and includes as special cases the exponential, the Log-normal, the Weibull, the Rayleigh, the Maxwell-Boltzmann, and the chi-square distributions. It is often used for modeling of the probability distribution for rare events. The GG PDF reads as follows:

$$P(x; a, \beta, p) = \frac{a x^{ap-1}}{\Gamma(p)\, \beta^{ap}} e^{-(x/\beta)^a}, \tag{5}$$

where a and p are known as the shape parameters, and β is the scale parameter. In our case the random variable x corresponds

to $x = |B_{\text{out}}|^2$ the peak intensity of the field in the random pattern.

The parameter estimation of this distribution is a mathematical problem in itself which still remains open [47]. We use a method of moments to evaluate the (a, β, p) parameters. For comparison, fitting regression methods (such as least squares) give multiple solutions for (a, β, p) and always lead to a poorer results. The idea is to equate the theoretical moments of the order r

$$E(x^r) = \beta^r \frac{\Gamma\left(p + \frac{r}{a}\right)}{\Gamma(p)} \tag{6}$$

to the ones calculated from the experimental data

$$E_{\text{data}}(x^r) = \frac{1}{n} \sum_{i=1}^{n} x_i^r, \tag{7}$$

where n is the number of peak maxima and x_i corresponds to the ith peak intensity of $|B_{\text{out}}|^2$. Solving numerically Eq. (6) = Eq. (7) for three moments provides us with (a, β, p). The best agreements are always obtained using the lowest moment orders.

The result of the modeling on a typical PDF using the GG distribution is given in Fig. 5. One can see the excellent agreement between the probability density function points and the GG curve for linear scale [Fig. 5(a)] as well as for log-linear scale [Fig. 5(b)]. It means that the GG distribution models low intensity peak distribution as well as intense ones.
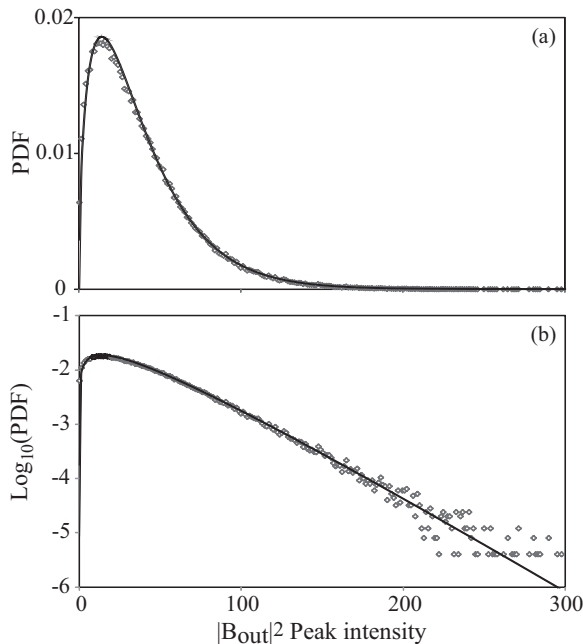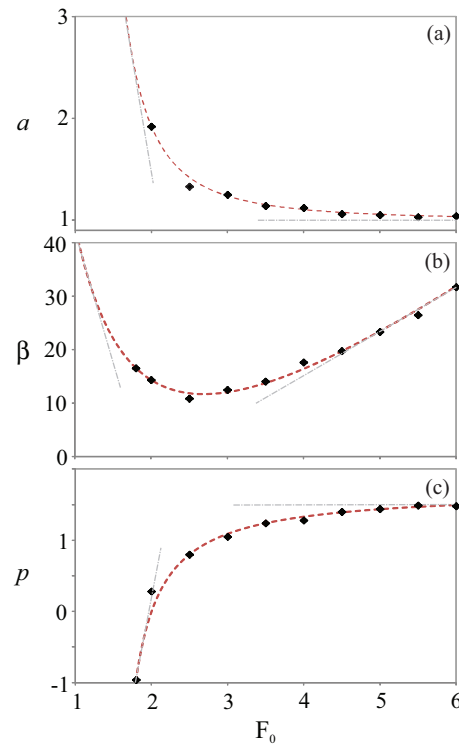
FIG. 5. Modeling of the numerical PDF of Fig. 2(h) using the generalized gamma distribution. (a) Linear and (b) $\log_{10}$ scale. Fitted GGD parameters (a, β, p) are 1.03, 26.47, and 1.49.

FIG. 6. (Color online) Evolution of the GGD parameters (a) a, (b) β, and (c) p versus pumping F_0. ◆, numerical points. The fit curves - are only plotted for a better reading. Asymptotic curves (in gray) indicate limit cases of no supercontinuum emission ($F_0 \lesssim 2$) and supercontinuum emission ($F_0 \gtrsim 4$) $R = 0.9$, $d = 5$ mm, $\chi = 1$, $w_x = 1400\ \mu$m.

In other words, the GG distribution perfectly reproduces the PDF curves.

The evolution of the GG (a, β, p) coefficients is reported in Fig. 6. One can notice a remarkable fact that the GG distribution converges to the gamma distribution ($a \rightarrow 1$) with the shape parameter equal to $3/2$ as the pump field F_0 reaches 4 to 5 and the supercontinuum emission is reached. We find this asymptotic behavior especially interesting because written in terms of the peak amplitudes $A = \sqrt{x}$ instead of the peak intensities, this probability density function just becomes—to a multiplicative constant—the Rayleigh distribution,

$$P(x = A^2; a = 1, \beta = 2\sigma^2, p = 3/2)$$
$$= \frac{1}{4\sqrt{\pi}\sigma^4} \frac{A}{\sigma^2} e^{-(A^2/2\sigma^2)} = \frac{1}{4\sqrt{\pi}\sigma^4} R(A, \sigma)$$

where $R(A, \sigma)$ is the Rayleigh distribution.

It is well known that this distribution of the wave amplitudes of the random oceanic waves corresponds to the Gaussian or normal statistics of such waves [43,44]. We can conclude, therefore, that in our case, very high above the Turing threshold, the statistics of the intensity peaks in the transverse patterns becomes Gaussian, which is a signature of random waves and the amount of incoherence in the system. Similar numerical investigation on the highly incoherent and nonlinear regime (and the emergence of rogue events) in a conservative system has been reported in [20].

The β coefficient confirms that increasing the input pump value F_0 gives rise to more intense extreme events as can be seen from Fig. 4 without changing the exponential dependence of the PDF tail. Thus, the evolution of these (a, β, p) coefficients can be used as quantitative indicators to follow the transition from the weakly nonlinear regime (close to the Turing threshold) to the regime of very high nonlinearity where supercontinuum emission and intense peaks are observed. As seen in Fig. 6, two asymptotic behaviors can be distinguished. One for $F_0 \lesssim 2$ and another one for $F_0 \gtrsim 4$ corresponding to the weakly and the highly nonlinear regimes, respectively. In the first case, the spatial frequency spectrum is composed of a cluster around the critical wave number k_{th} of the Turing instability together with its harmonics. For the second regime, the spectrum always displays a continuum band that dominates the spectrum partially or totally.

V. EXPERIMENTS

The experimental recordings are achieved via a CCD camera with an 8-bit resolution depth that is imaging the near-field intensity (i.e., within the liquid crystal cell). At modulational instability threshold the transverse wavelength is 100 μm and the pumping beam diameter is 3200 μm so that
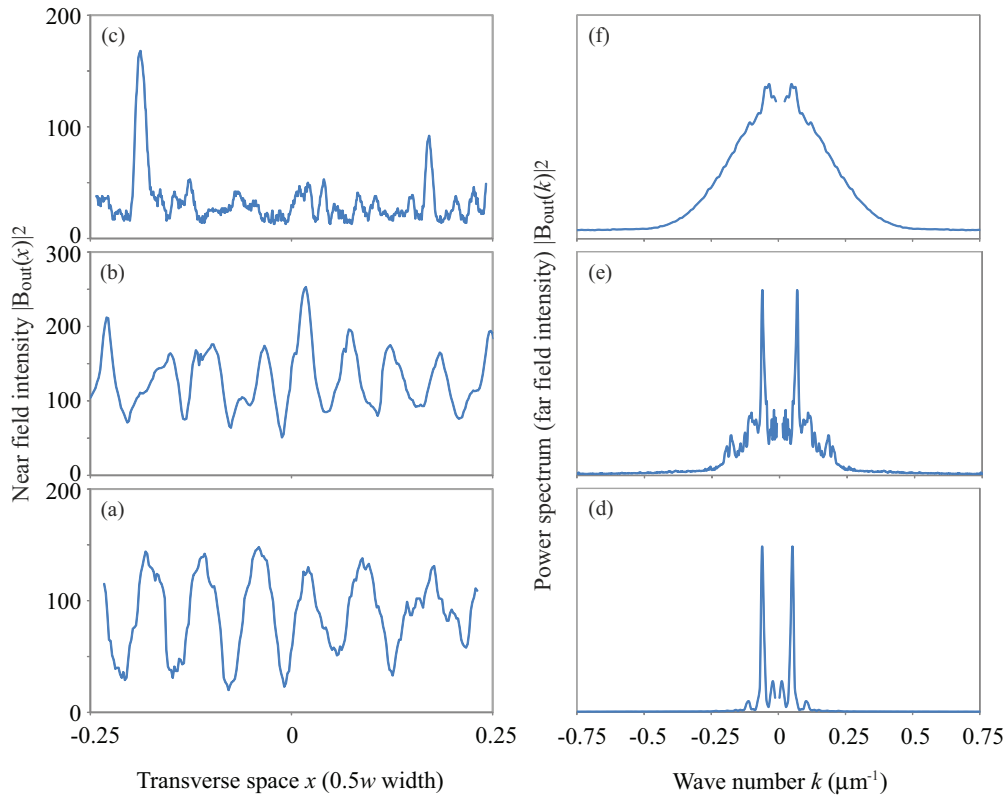

FIG. 7. (Color online) Experimental evolution of the (a)–(c) near and (d)–(f) far-field profiles of the transverse pattern for the transition from the [(a), (d)] weak nonlinear regime (close to the primary threshold of the modulational instability) to the [(c), (f)] highly nonlinear one (supercontinuum emission). [(a),(d)] $I_0 = 132$ W cm^{-2}, $I_0/I_{th} = 1$, [(b),(e)] $I_0 = 265$ W cm^{-2}, $I_0/I_{th} = 2$, and [(c),(f)] $I_0 = 1193$ W cm^{-2}, $I_0/I_{th} = 9$. $R = 0.9$, $d = 5$ mm, $w_x = 1600$ μm. Power spectra (far fields) (d)–(f) are averaged over the experimental recording sequence (typically 1000 s). (a)–(c) correspond to the time when the near-field highest intensity is detected for the associated recording. For (e)–(h) plots, the $k = 0$ component has been suppressed and the power spectra rescaled.

the aspect ratio is around 30. In order to follow the condition on the restricted spatial zone D_x of the Gaussian input pump used to plot the PDFs, we record a near-field region whose width is $D_x \sim 0.5w$ centered on the top of the Gaussian pump profile.

A. Spectral continuum

Close to the primary threshold of modulational instability (very weak nonlinear regime), the near-field profile is almost periodic [Fig. 7(a)] with a wave number $k_{th} = 63$ mm^{-1} [Fig. 7(d)] in agreement with the ones predicted by the theory $k_{th}(theo) = \pm 61$ mm^{-1} and numerics $k_{th}(num) = 59.8$ mm^{-1}. Increasing the pump power, this modulation transforms into sharp peaks, indicating the presence of harmonics of k_{th} as shown in [Fig. 7(e)]. Increasing further I_0 to many times the primary threshold I_{th}, the highly nonlinear regime is reached. In this latter case, the spatial power spectrum (far field) always depicts a continuum of spatial frequencies [Fig. 7(f)]. This continuum is completely similar to the ones obtained for numerical simulations as can be checked in Fig. 2(h). Its width (half width at half maximum) reaches approximately, e.g., eight times the wave number k_{th} at modulational instability threshold for $I_0/I_{th} = 9$.

B. Statistical analysis

The near field associated with the emission of spectral supercontinuum [Fig. 7(f)] depicts intense and rare localized patterns whose peak amplitude can reach 2.1 times the significant peak amplitude for, e.g., $I_0/I_{th} = 6$ (Fig. 8). These localized states occur suddenly with a lifetime smaller than 0.5 s (to compare with the characteristic time $\tau = 2.28$ s of the dynamics).

A typical PDF obtained for supercontinuum emission is plotted on Fig. 8 in linear and logarithmic scales for $I/I_{th} = 6$. We can see that it is completely similar to the one predicted in Fig. 3 and that the GG function perfectly models the PDF curves. The value of the fitted parameters ($a = 1.13$, $\beta = 21.06$, $p = 1.3$) of the GG distribution model agrees with the numerical ones obtained for a similar intensity pumping ratio (experimentally, $I/I_{th} = 6$). More precisely, the experimental tail of the PDF follows the same concavity as the prediction, namely, $a = 1.13 \pm 0.02$.

Determination of the (a, β, p) coefficients of the GG function from the experimental data, even with the moment method (Sec. IV B 2), remains a complicated problem. In our case, as can be seen on the transverse profile of the beam [Fig. 8(c)], the experimental recording is noisy. Therefore, we smoothed the profile using the Savitsky-Golay convolution method [48]. Then, a least-square method provides us with the optimum number of neighboring points to include in the smoothing.

The only experimental restriction to reach values of I/I_{th} higher than 6 is that our pumping is 1D-like so that for the high pump input intensities, the beam starts to self-focus and it expands in the transverse orthogonal direction to the 1D axis [49]. The local intensity in the center of the beam then reaches a plateau and saturates. Thus, it is not possible in our setup to reach more than typically six to eight times
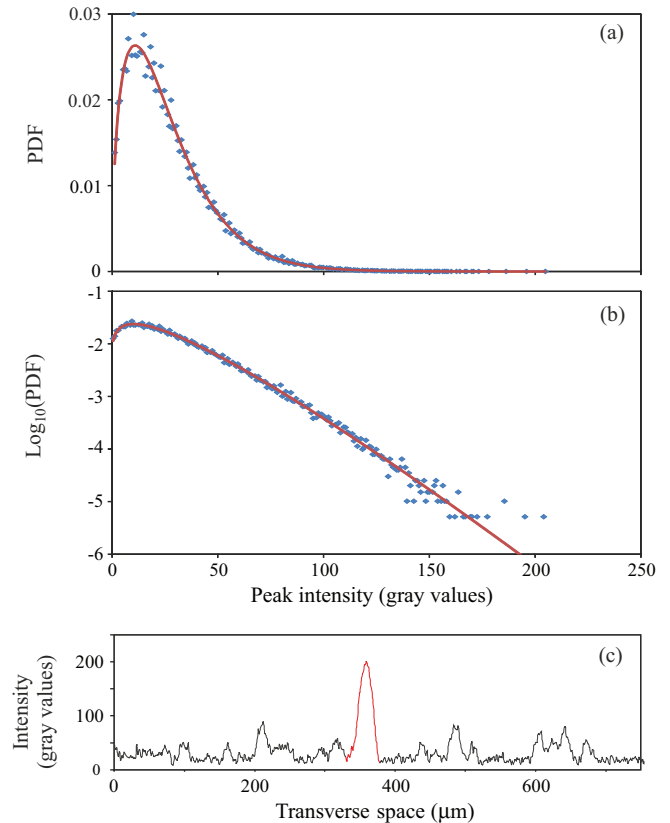

FIG. 8. (Color online) (a) Experimental PDF of intensity peaks obtained in the transverse pattern of Fig. 1. (b) PDF in log$_{10}$ scale. (c) Typical spatial extreme event. $w = 1600$ μm. Input intensity is six times intensity threshold I_{th}.

the threshold for the modulation instability so that the full convergence of the PDF to the gamma distribution with $a = 1$ cannot be completely achieved. Nevertheless, our experiments are sufficient to evidence the decreasing of parameter a and generation of experimental spatial supercontinuum and intense localized peaks.

VI. CONCLUSION

We have numerically and experimentally evidenced generation of a spectral supercontinuum in the highly nonlinear regime of a spatially extended feedback system. This regime, obtained for the input beam intensities far above the threshold of the Turing instability, possesses a very complex spatiotemporal dynamics that depicts the emission of intense localized peaks. This spectral broadening can be seen as a spatial counterpart of the supercontinuum generation in temporal fiber systems. Using a statistical approach, we characterized the transition from a weakly to a highly nonlinear regime using probability density functions of the intensity peaks. Their modeling with the generalized gamma distribution provides us with parameters that are used as quantitative indicators to investigate the transition to the highly nonlinear regime. In our case, the GG distribution parameters show that the PDF converges to the gamma distribution when approaching the highly nonlinear regime. Finally, the study of spectral broadening leading to the continuum is a challenge to identify

its mechanism such as, e.g., energy cascades in the case of weak turbulence theory [50].

APPENDIX: INFLUENCE OF THE GAUSSIAN PUMPING PROFILE ON THE PDFs

We describe how we calculate the PDFs in our particular case of a Gaussian transverse pumping.

Let us remember that the PDF is the histogram of the peak intensities recorded along the spatial pattern. It is clear that even if the PDFs calculated, e.g., in the central part and in the wings of a Gaussian pump have the same profile, putting them into a unique histogram will completely change the
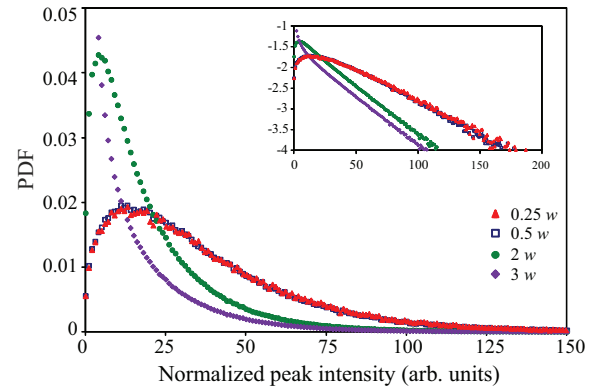

FIG. 9. (Color online) (a) Influence of the analyzed zone size on the PDF in the case of a Gaussian pumping profile. The inset is the PDF in log-linear scale. $F_0 = 6$. Same parameters as Fig. 2.

shape of the resulting PDF. Thus, it is important to plot PDFs for uniformlike pumping conditions. To this end we performed all our PDF calculations on a restricted spatial zone D_x of the Gaussian input pump. This area is located in the central part and its extension can vary between 0.25 and 0.5w, with 2w the beam diameter. This allows intensity variations lower than 1.5 to 6% along the area D_x. The choice of this extension size is given by the PDF modification versus different sizes of the analyzed domain D_x. Indeed, we can see in Fig. 9 that the features of the PDF remain unchanged until D_x is smaller than 0.5w, and change versus D_x in the other case. In this paper, we calculate all our PDFs verifying this condition.

[1] C. Kharif and E. Pelinovsky, Eur. J. Mech. B/Fluids **22**, 603 (2003).

[2] W. Broad, The New York Times (July 11, 2006).

[3] F. Fedele, Phys. D: (Amsterdam, Neth.) **237**, 2127 (2008), Euler Equations: 250 Years On - Proceedings of an International Conference [http://www.sciencedirect.com/science/article/B6TVK-4RR1NMH-2/2/7e428b0e9591617b805edeea29f554f1].

[4] J.-W. Kim and E. Ott, Phys. Rev. E **67**, 026203 (2003).

[5] L. Du, Q. Chen, Y.-C. Lai, and W. Xu, Phys. Rev. E **78**, R015201 (2008).

[6] J. Dudley, G. Genty, and B. Eggelton, Opt. Express **16**, 3644 (2008).

[7] D. R. Solli, C. Ropers, P. Koonath, and B. Jalali, Nature (London) **450**, 1054 (2007).

[8] K. Hammani, C. Finot, J. M. Dudley, and G. Millot, Opt. Express **16**, 16467 (2008).

[9] A. Mussot, A. Kudlinski, M. Kolobov, E. Louvergneaux, M. Douay, and M. Taki, Opt. Express **17**, 17010 (2009).

[10] A. Montina, U. Bortolozzo, S. Residori, and F. T. Arecchi, Phys. Rev. Lett. **103**, 173901 (2009).

[11] J. Kasparian, P. Béjot, J. Wolf, and J. Dudley, Opt. Express **17**, 12070 (2009).

[12] V. Odent, M. Taki, and E. Louvergneaux, Nat. Hazards Earth Syst. Sci. **10**, 2727 (2010).

[13] F. T. Arecchi, U. Bortolozzo, A. Montina, and S. Residori, Phys. Rev. Lett. **106**, 153901 (2011).

[14] S. Residori, U. Bortolozzo, A. Montina, F. Lenzini, and F. T. Arecchi, Fluct. Noise Lett. **11**, 1240014 (2012).

[15] G. P. Agraval, *Nonlinear Fiber Optics* (Academic Press, San Diego, California, 1995).

[16] V. E. Zakharov, J. Appl. Mech. Tech. Phys. **9**, 190 (1968).

[17] M. Onorato, A. R. Osborne, M. Serio, and S. Bertone, Phys. Rev. Lett. **86**, 5831 (2001).

[18] S. Massel, *Ocean Surface Waves: Their Physics and Prediction* (World Scientific, Singapore, 1996).

[19] J. M. Dudley, G. Genty, and S. Coen, Rev. Mod. Phys. **78**, 1135 (2006).

[20] B. Kibler, K. Hammani, C. Michel, C. Finot, and A. Picozzi, Phys. Lett. A **375**, 3149 (2011).

[21] M. Onorato, S. Residori, U. Bortolozzo, A. Montina, and F. Arecchi, Phys. Rep. (to be published).

[22] R. Neubecker, B. Thuring, M. Kreuzer, and T. Tschudi, Chaos, Solitons Fractals **10**, 681 (1999).

[23] L. Pastur, U. Bortolozzo, and P. L. Ramazza, in *Experimental Characterization of Space-Time Chaos in Nonlinear Optics*, AIP Conf. Proc. No. 676 (AIP, Melville, NY, 2003), pp. 182–188.

[24] J. Laurie, U. Bortolozzo, S. Nazarenko, and S. Residori, Phys. Rep. **514**, 121 (2012).

[25] N. Akhmediev and E. Pelinovsky, Eur. Phys. J.: Spec. Top. **185**, 1 (2010).

[26] N. Akhmediev, A. Ankiewicz, and M. Taki, Phys. Lett. A **373**, 675 (2009).

[27] G. D'Alessandro and W. J. Firth, Phys. Rev. A **46**, 537 (1992).

[28] E. Louvergneaux, Phys. Rev. Lett. **87**, 244501 (2001).

[29] W. J. Firth, J. Mod. Opt. **37**, 151 (1990).

[30] S. Akhmanov, M. Vorontsov, and V. Y. Ivanov, JETP Lett. **47**, 707 (1988).

[31] C. Denz, M. Schwab, M. Sedlatschek, T. Tschudi, and T. Honda, J. Opt. Soc. Am. B **15**, 2057 (1998).

[32] F. Arecchi, S. Boccaletti, S. Ducci, E. Pampaloni, P. Ramazza, and S. Residori, J. Nonlinear Opt. Phys. Mater. **9**, 183 (2000).

[33] T. Ackemann and W. Lange, Appl. Phys. B **72**, 21 (2001).

[34] G. Agez, P. Glorieux, M. Taki, and E. Louvergneaux, Phys. Rev. A **74**, 043814 (2006).

[35] P. L. Ramazza, S. Ducci, S. Boccaletti, and F. T. Arecchi, J. Opt. B: Quantum Semiclassical Opt. **2**, 399 (2000).

[36] U. Bortolozzo and S. Residori, Phys. Rev. Lett. **96**, 037801 (2006).

[37] J. P. Sharpe, P. L. Ramazza, N. Sungar, and K. Saunders, Phys. Rev. Lett. **96**, 094101 (2006).

[38] M. C. Cross and P. C. Hohenberg, Rev. Mod. Phys. **65**, 851 (1993).

[39] K. Tai, A. Hasegawa, and A. Tomita, Phys. Rev. Lett. **56**, 135 (1986).

[40] G. Genty, M. Surakka, J. Turunen, and A. T. Friberg, J. Opt. Soc. Am. B **28**, 2301 (2011).

[41] L. E. Hooper, P. J. Mosley, A. C. Muir, W. J. Wadsworth, and J. C. Knight, Opt. Express **19**, 4902 (2011).

[42] N. Akhmediev, J. Soto-Crespo, and A. Ankiewicz, Phys. Lett. A **373**, 2137 (2009).

[43] N. Mori and P. A. E. M. Janssen, J. Phys. Oceanogr. **36**, 1471 (2006).

[44] N. Mori and T. Yasuda, Ocean Engineering **29**, 1219 (2002).

[45] K. Hammani, A. Picozzi, and C. Finot, Opt. Commun. **284**, 2594 (2011).

[46] E. Stacy, Ann. Math. Stat. **33**, 1187 (1962).

[47] O. Gomes, C. Combes, and A. Dussauchoy, Math. Comput. Simul. **79**, 955 (2008); 5th Vienna International Conference on Mathematical Modelling/Workshop on Scientific Computing in Electronic Engineering of the 2006 International Conference on Computational Science/Structural Dynamical Systems: Computational Aspects, http://www.sciencedirect.com/science/article/B6V0T-4RTW3S3-5/2/cbb24faa453cc1409fcf044b630159f0.

[48] A. Savitzky and M. J. E. Golay, Anal. Chem. **36**, 1627 (1964).

[49] I. Khoo, *Liquid Crystals: Physical Properties and Nonlinear Optical Phenomena* (Wiley, New York, 1995).

[50] V. Zakharov, V. Lvov, and G. Falkovich, *Kolmogorov Spectra of Turbulence*, Sec. A (Springer-Verlag, Berlin, 1992).